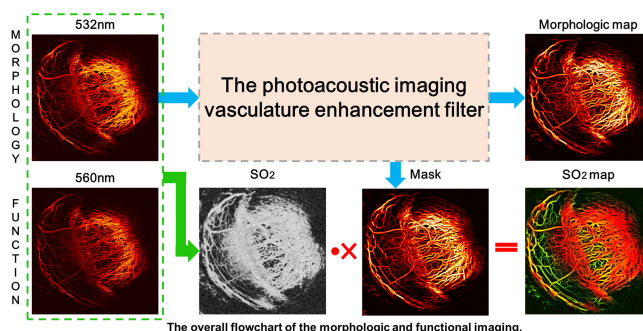


# Multiscale Vascular Enhancement Filter Applied to *In Vivo* Morphologic and Functional Photoacoustic Imaging of Rat Ocular Vasculature





Volume 11, Number 06, December 2019

Huangxuan Zhao  
Ke Li  
Ningbo Chen  
Kunya Zhang  
Lidai Wang  
Riqiang Lin  
Xiaojing Gong  
Liang Song  
Zhicheng Liu  
Chengbo Liu



DOI: 10.1109/JPHOT.2019.2948955

# Multiscale Vascular Enhancement Filter Applied to *In Vivo* Morphologic and Functional Photoacoustic Imaging of Rat Ocular Vasculature

Huangxuan Zhao <sup>1,2,3</sup>, Ke Li,<sup>1,2,3</sup> Ningbo Chen <sup>2</sup>, Kunya Zhang,<sup>1,3</sup>  
Lidai Wang,<sup>4</sup> Riqiang Lin,<sup>2</sup> Xiaojing Gong <sup>2</sup>, Liang Song,<sup>2</sup>  
Zhicheng Liu,<sup>1,3</sup> and Chengbo Liu <sup>2</sup>

<sup>1</sup>School of Biomedical Engineering, Capital Medical University, Beijing 100069, China

<sup>2</sup>Research Laboratory for Biomedical Optics and Molecular Imaging, Shenzhen Institutes of Advanced Technology, Chinese Academy of Sciences, Shenzhen 518055, China

<sup>3</sup>Beijing Key Laboratory of Fundamental Research on Biomechanics in Clinical Application, Beijing 100069, China

<sup>4</sup>Department of Mechanical and Biomedical Engineering, City University of Hong Kong, 83 Tat Chee Ave, Kowloon, Hong Kong SAR, China

DOI:10.1109/JPHOT.2019.2948955

This work is licensed under a Creative Commons Attribution 4.0 License. For more information, see <https://creativecommons.org/licenses/by/4.0/>

Manuscript received September 26, 2019; revised October 18, 2019; accepted October 18, 2019. Date of publication October 22, 2019; date of current version November 26, 2019. This work was supported in part by the National Natural Science Foundation of China (NSFC) under Grants 91739117, 31570952, 81430038, and 81427804, in part by the National Key Basic Research (973) Program of China under Grant 2015CB755500, in part by Beijing Natural Science Foundation under Grant 3122010, in part by Guangdong Natural Science Foundation under Grant 2014A030312006, in part by Shenzhen Science and Technology Innovation under Grants JCYJ20170413153129570 and JCYJ20160608214524052, in part by Guangzhou Science and Technology Innovation under Grant 201604020144, and in part by the Chinese Academy of Sciences under Grants GJJSTD20180002 and SKLA-2018-03. Corresponding authors: (e-mails: Zhicheng Liu: zcliu@ccmu.edu.cn; Chengbo Liu: cb.liu@siat.ac.cn).

**Abstract:** Optical-resolution photoacoustic microscopy (OR-PAM) is used for *in vivo* imaging of a variety of albino and pigmented eyes taking advantages of requiring no exogenous dye, performing high-resolution imaging, and achieving morphologic and functional imaging at the same time. However, to accurately diagnose the ophthalmic disease in the OR-PAM images, vascular enhancement algorithms are necessary for extracting vessels and quantifying them correctly. Vascular enhancement algorithms developed for other imaging technologies, are not suitable to be used for OR-PAM, because of the underlying differences in the physics of the formation of images. In this study, a new vascular enhancement algorithm called photoacoustic imaging vasculature enhancement filter (PAIVEF) is proposed, which not only enhances vasculature including micro-vessels signals, suppresses noise signals effectively, but also achieves highly sensitive and accurate enhancement of the vasculature within a large depth range in and out of the system's depth of focus (DOF). Using the PAIVEF, the morphologic and functional 3D images of the whole rat's ocular anterior vasculature segment was displayed simultaneously for a depth range of ~0.6 mm, which was ~7 times of the system's DOF. This study paves the way for the application of OR-PAM technology in ophthalmic disease research.

**Index Terms:** Photoacoustic imaging, vascular enhancement filter, morphologic and functional imaging, ocular vasculature.

## 1. Introduction

Ophthalmic diseases are very prevalent throughout the world and pose a serious threat to the society [1], [2]. Studies have shown that glaucoma, cataract, and ocular vascular diseases are all accompanied by changes in the blood microcirculation in the anterior segment of the eye. Monitoring the changes of blood microcirculation in the anterior segment is of great importance [3]–[5]. The current standard of care, fluorescence imaging (FA) and optical coherence tomography angiography (OCTA) imaging are not ideal due to several reasons. The FA method, which needs injection of external contrast agents, has many limitations: (1) On the one hand, if the diameters of contrast agent particles are too small, they will leak through vessels; on the other hand, if the particles are large, the speckles dominate the image making it difficult to identify the microvessels. (2) Contrast agents cannot reach blocked lesions. (3) Contrast agents are not only painful to patients while administering, they also cause nausea, vomiting and allergies in almost 10% of patients [6], [7]. The OCTA obtains ocular blood vessels images through the Doppler Effect and is widely used in the diagnosis of fundus diseases [8]–[10]. However, due to the slow blood flow velocity, the imaging quality in the anterior segment is suboptimal [11]–[13]. A new biomedical imaging device called optical resolution photoacoustic microscopy (OR-PAM), which images both morphological and functional images of small micro-blood vessels with high fidelity and uses no external agent, is now being considered as a promising modality to study varieties of ophthalmic diseases.

Currently, OR-PAM is widely used in preclinical research, e.g., studies of tumor [14], brain [15], [16] and skin tissues [17], [18]. A nanosecond pulsed laser is generally applied to shed laser into the biological tissues. The absorbed laser energy by the chromophores (such as oxy- and deoxy- hemoglobin in blood vessels) in the tissue generates acoustic waves through the process of laser energy absorption, instantaneous temperature rise, transient thermoelastic expansion, and acoustic wave emission. These generated acoustic waves (also termed as photoacoustic signals) are captured by an ultrasound transducer to form a photoacoustic image [19], [20]. The anterior parts of the eye are very suitable for OR-PAM application due to the optical transparency of the eye [19], [21]. Recently, this technique has been used to evaluate in living albino and pigmented eyes and has obtained super image qualities of anterior parts even in the diseased eyes [21]–[29].

As other optical imaging methods, photoacoustic imaging also encounters the challenges such as unknown optical parameters (e.g., absorption and scattering coefficients) of the biological sample, variation of the vascular information with respiration, and heterogeneous distribution of the blood vessels. Hence accurate simulation of optical fluence is very important to quantitative photoacoustic imaging, such as when extracting sO<sub>2</sub> functional information [30], [31]. In addition to that, enhancing the vascular signals through image processing is also critically important for efficient disease diagnosis and monitoring. Several state-of-the-art vascular enhancement filters have been proposed for magnetic resonance angiography (MRA), computed tomography angiography (CTA), digital subtraction angiography (DSA), etc. [32]–[34]. However, these algorithms are not suitable to be extended directly to OR-PAM because differences in underlying physics in the formation of images lead to different sensitivities and signal to noise ratio (SNR) in images. The Frangi's filter [35], which is the most popular vascular enhancement algorithm used in many kinds of optical imaging systems [36]–[39], has low tolerance to noise of the OR-PAM images. We applied this filter to OR-PAM by combining it with morphological processing in our previous publication [40], and achieved better results. But there are still two problems affecting the accuracy of vascular enhancement: (1) The morphological processing suppresses microvascular signals, which are invaluable in disease diagnosis. (2) The previous method has limited enhancement of blood vessels in defocus areas. As the depth of focus (DOF) of conventional OR-PAM only covers less than 100  $\mu\text{m}$ , it is not enough for curved sample imaging such as the whole anterior of the eyeball. Depth scanning may be considered to solve the second problem, but will restrain the imaging speed [41], [42].

In this study, we proposed a new vascular enhancement algorithm, called photoacoustic imaging vasculature enhancement filter (PAIVEF) specifically targeting OR-PAM imaging, which not only enhance microvascular signals while suppressing high frequency noise, but also achieve highly sensitive and accurate enhancement of the vasculature at a much larger depth range ( $\sim 7$  times of

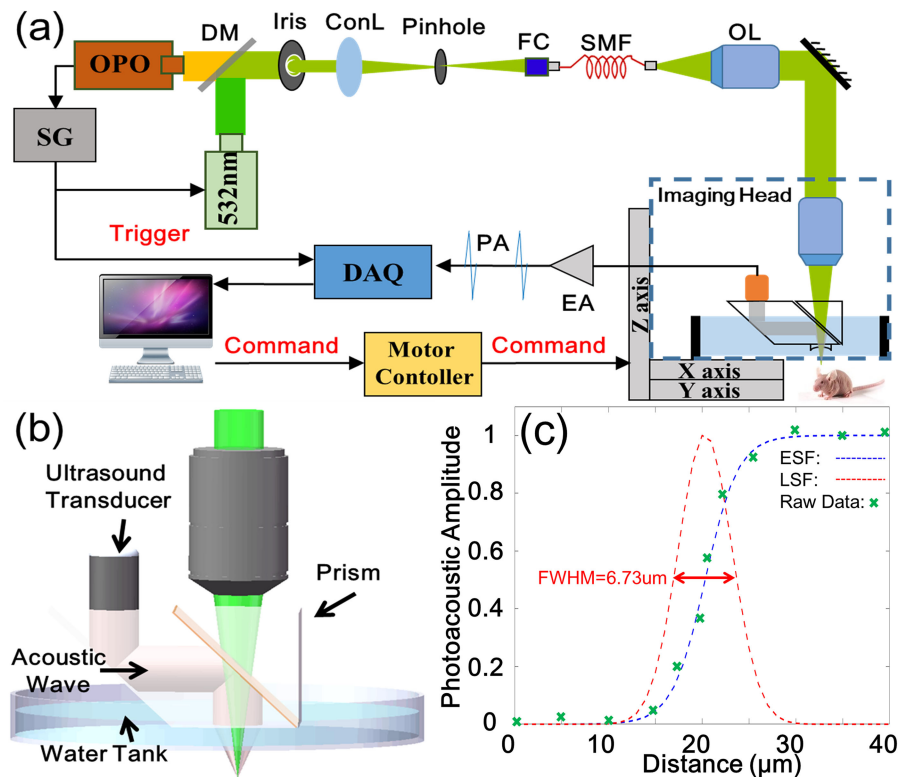


Fig. 1. (a) Schematic of the custom-built OR-PAM. SG: signal generator, DM: dichroic mirrors, ConL: condenser lens, FC: fiber collimator, SMF: single-mode fiber, OL: objective lens, DAQ: data acquisition card. (b) The enlarged view of imaging head. (c) Estimating result of the full width at half maximum (FWHM) using the edge of a sharp metallic blade. Green cross: original photoacoustic signals; blue dash line: edge spread function (ESF); red dash line: the first-order derivative of the ESF, representing the LSF along the scanning direction.

the system's DOF). Using the PAIVEF, the morphologic and functional 3D images of the rat's whole ocular anterior vasculature in and out of the system's DOF were displayed simultaneously.

## 2. Materials and Methods

### 2.1 Experimental System

We modified a custom-built OR-PAM system described in [40], [43] to obtain high resolution morphological and functional imaging of the vasculature in rat's ocular anterior segment. The system schematic is shown in Fig. 1(a), with appropriate modifications made to the optical path and control sequence of OR-PAM to achieve functional imaging, as compared to our previous design. In brief, an optical parametric oscillator (OPO) pulsed laser (NT-242, Ekspla, Vilnius, Lithuania, a wavelength of 560 nm was used in here) and a 532 nm pulsed laser (GKNQL-532, Beijing Guoke Laser Co., Beijing, China) both with a repetition rate of 1 kHz were used as the illumination source. The two output laser beams are first converged by a dichroic mirror (DM), which reflects the 532 nm light and transmits the 560 nm light, and then reshaped by an iris (ID25SS, Thorlabs; 2 mm aperture size). The reshaped beam gets focused by a condenser lens (LA1131, Thorlabs) before passing through a 50  $\mu\text{m}$  pinhole (P50C, Thorlabs), and launched into a single-mode fiber (P1-460A-FC-2, Thorlabs) coupled to the fiber coupler (F-91-C1, Newport). The output of the single-mode fiber is first collimated by an objective lens (RMS4X, Thorlabs), and then reflected by a stationary mirror to fill the back aperture of another identical objective lens (imaging objective) to achieve optical focusing.

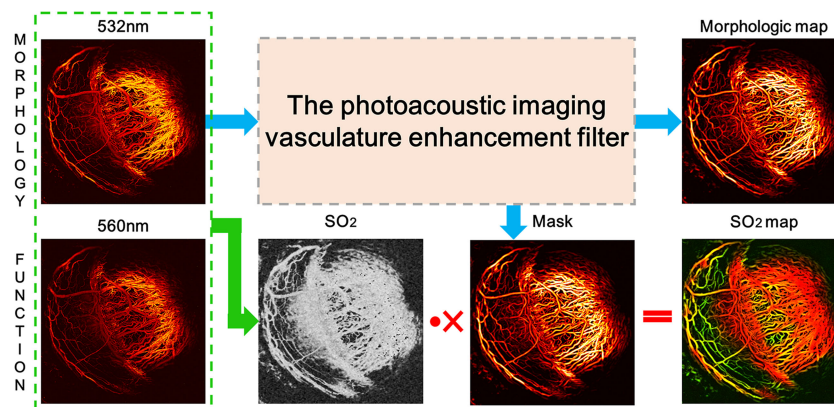


Fig. 2. The overall flowchart of the morphologic and functional imaging.

The focused spot is illuminated on the imaging sample to generate photoacoustic signals, which are then collected by a single element ultrasound transducer (V2022, Olympus-NDT, Kennewick, WA, USA). The acquired signals were further amplified by an amplifier and transmitted to the data acquisition card (CS1422, Gage Applied Technologies Inc., Lockport) for three-dimensional (3D) reconstruction when synchronized with 3D mechanical scanning. For functional imaging, to accurately measure sO<sub>2</sub>, an optimum 10  $\mu$ s trigger delay was applied to the 532 nm laser compared to the OPO laser to ensure no interference occurs between the two photoacoustic signals and also to ensure the delay causes least changes in blood functional information. The imaging head of OR-PAM (enlarged in Fig. 1(b)) as described in [40] consists of a set of individually designed prisms, a water tank, an objective lens, and a single element ultrasound transducer. The lateral resolution of our system was  $\sim 6.73 \mu\text{m}$  (showed in Fig. 1(c)) by measuring the edge of a sharp metallic blade.

## 2.2 Animal Preparation and Experiment

We selected one 8 weeks old healthy female Sprague Dawley rat (320 g) for photoacoustic imaging. The rat remained anesthetized throughout the experiment using 1.5% isoflurane gas (Euthanex, Palmer, Pennsylvania) mixed with oxygen. The rat's right eyelid was flipped inside out and fixed with a custom designed fixation device to expose the eyeball. Coupling glue was applied to the imaging area of the eyeball, and the imaging head of the custom-built OR-PAM was positioned directly above it. The surface laser fluence is below 11 mJ/cm<sup>2</sup>, which is within the American National Standards Institute safety limit [22], [27]. The animal handling and experimental procedures were approved by the Animal Study Committee of Shenzhen Institutes of Advanced Technology, Chinese Academy of Sciences.

## 2.3 Overall Morphologic and Functional Imaging

In this section, we present the flow chart of our vascular enhancement filter applied to morphological and functional imaging. As shown in Fig. 2, the 3D data with 532 nm and 560 nm wavelength were obtained using our custom-built OR-PAM system. The raw image data obtained using 532 nm wavelength was imported into our vascular enhancement filter to obtain enhanced vasculature data, which is then used for morphological analysis and also as a mask for functional imaging. During the functional imaging, the sO<sub>2</sub> values at each pixel location in the two images acquired at 532 nm and 560 nm wavelengths are calculated based on the raw data. These sO<sub>2</sub> values are calculated in conjunction with the mask. The details of vascular enhancement filter and sO<sub>2</sub> calculation method are further described in Part 2.4 and 2.5.

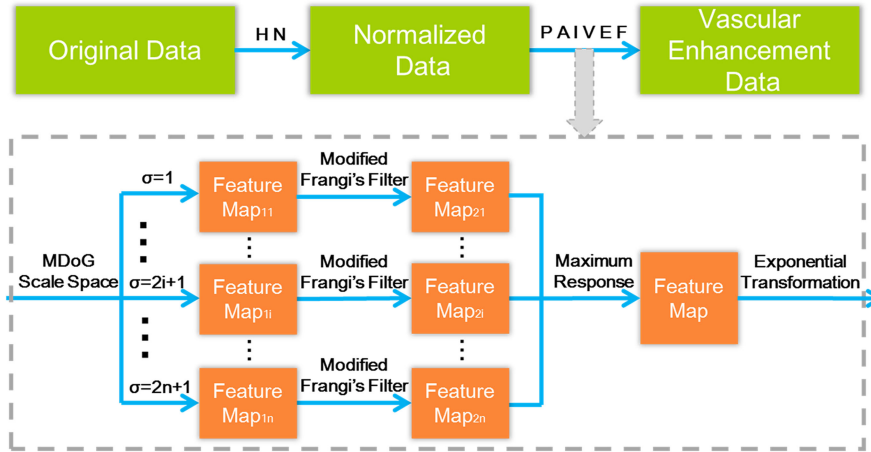


Fig. 3. The overall flowchart of the algorithm. HN: Histogram Normalization.

## 2.4 Photoacoustic imaging vasculature enhancement filter (PAIVEF)

**2.4.1 Overall Algorithm:** The overall flow chart of the algorithm is shown in Fig. 3. First, the raw data is normalized before applying our newly developed PAIVEF algorithm to enhance vascular signals. The details of PAIVEF algorithm are outlined in Fig. 3 by the grey dotted box. The main innovations of PAIVEF include: (1) Difference of Gaussians scale space was modified and established in here to smooth vessels, while preparing for multiscale vascular enhancement (obtaining Feature Map<sub>11</sub> to Feature Map<sub>1n</sub>), named as MDoG scale space; (2) Enhancing all vasculature signals with modified Frangi's filter (Feature Map<sub>21</sub> to Feature Map<sub>2n</sub>); (3) Obtaining the final Feature Map using maximum response function, and then further enhancing the microvasculature signals by exponential transformation to obtain the final vascular enhancement data. (4) The modified Frangi's filter has reduced computation complexity taking less time to apply the filter. The step-by-step implementation of our technique is described in Section 2.4.2–2.4.5. All the post-processing of the acquired data was performed using MATLAB (R2017a, Mathworks, Natick, MA, USA) on a PC with Xeon Silver 4110 Central Processing Unit (CPU) and a 64GB RAM.

**2.4.2 Overall Algorithm:** The MDoG scale space is developed to smooth the blood vessels in the multi-scale feature map and to eliminate high-frequency noise signals introduced by the system and sample. The feature maps in the MDoG scale space are calculated by convolving the normalized input data with MDoG detector:

$$F(x, y, z, \sigma) = N(x, y, z) * d(x, y, z, \sigma) \quad (1)$$

where  $\sigma$  is the Gaussian scale factor,  $*$  denotes the convolution operator,  $N(x, y, z)$  is the normalized data and  $d(x, y, z, \sigma)$  is the MDoG detector. We define MdoG filter as follows:

$$d(x, y, z, \sigma) = \begin{cases} |G(x, y, z, k\sigma) - G(x, y, z, \sigma)|, & \text{if } G(x, y, z, k\sigma) - G(x, y, z, \sigma) \leq 0; \\ 0, & \text{if } G(x, y, z, k\sigma) - G(x, y, z, \sigma) > 0. \end{cases} \quad (2)$$

where  $G(x, y, z, \sigma) = \frac{1}{2\pi\sigma^2} e^{-(x^2+y^2+z^2)/2\sigma^2}$  is the Gaussian kernel function and  $k$  is a constant multiplicative factor, which is set to  $k = 1.2$ . Different feature maps in the images are obtained by varying  $\sigma$ . In our study, we vary  $\sigma$  from 1 to 9 to obtain different feature maps describing the vasculature in the image. More details on feature maps are provided in the next section.

**2.4.3 Modified Frangi's Filter:** Our modified Frangi's filter enhances the whole vasculature signals present in the 3D volume, by calculating 3D Hessian matrix at each data point of the 3D volume. The 3D Hessian matrix is a  $3 \times 3$  matrix at each data point in the 3D volume consisting of second-order

partial derivative of  $F(x, y, z, \sigma)$ :

$$\nabla^2 F = \begin{pmatrix} \frac{\partial^2 F(x,y,z,\sigma)}{\partial x^2} & \frac{\partial^2 F(x,y,z,\sigma)}{\partial x \partial y} & \frac{\partial^2 F(x,y,z,\sigma)}{\partial x \partial z} \\ \frac{\partial^2 F(x,y,z,\sigma)}{\partial y \partial x} & \frac{\partial^2 F(x,y,z,\sigma)}{\partial y^2} & \frac{\partial^2 F(x,y,z,\sigma)}{\partial y \partial z} \\ \frac{\partial^2 F(x,y,z,\sigma)}{\partial z \partial x} & \frac{\partial^2 F(x,y,z,\sigma)}{\partial z \partial y} & \frac{\partial^2 F(x,y,z,\sigma)}{\partial z^2} \end{pmatrix} \quad (3)$$

where  $F(x, y, z, \sigma)$  is the feature maps in the MDoG scale space. The steps to identify and enhance vascular signals using above Hessian matrix are described in the next two paragraphs.

At first, the vascular signals are identified by calculating three dominant eigenvalues ( $\lambda_1, \lambda_2, \lambda_3$ ) of the Hessian matrix. Three orthogonal vectors ( $e_1, e_2, e_3$ ) are chosen as the eigenvectors of the Hessian matrix, with each eigenvector representing one of the orthogonal directions. The direction with minimal value descendent of  $F(x, y, z, \sigma)$  is chosen as the axial direction of the blood vessel with the other two representing the other two orthogonal directions. Since the image feature along the direction of the blood vessels does not change substantially, the eigenvalue  $\lambda_1$  corresponding to this direction has minimum value and is close to 0. The other two eigenvalues,  $\lambda_2$  and  $\lambda_3$ , corresponding to other two orthogonal radial directions are close in value to each other ( $|\lambda_2| \leq |\lambda_3|$ ) and their absolute values are much larger than that of  $\lambda_1$ . Since the vascular signal in the photoacoustic imaging data is higher than the background signal,  $\lambda_2$  and  $\lambda_3$  are less than 0. Thus, the vascular signals in the 3D volume data are identified using the following criteria:

$$|\lambda_1| \ll |\lambda_2|; \quad \lambda_2 \approx \lambda_3 < 0; \quad (4)$$

In the second step, identified vascular signals are enhanced while suppressing other signals. The Frangi's filter defined in [35] is reproduced here:

$$I(\sigma) = \begin{cases} 0, & \lambda_2 > 0 \text{ or } \lambda_3 > 0 \\ \left(1 - \exp\left(-\frac{RA^2}{2\alpha^2}\right)\right) \exp\left(-\frac{RB^2}{2\beta^2}\right) \times \left(1 - \exp\left(-\frac{S^2}{2\gamma^2}\right)\right), & \text{else} \end{cases} \quad (5)$$

where  $RA = |\lambda_2|/|\lambda_3|$ ,  $RB = |\lambda_1|/\sqrt{|\lambda_2\lambda_3|}$ ,  $S = \sqrt{\lambda_1^2 + \lambda_2^2 + \lambda_3^2}$ .  $\alpha, \beta$  and  $\gamma$  are thresholds to control the sensitivity of the filter to  $RA, RB$  and  $S$  for removing non-vascular signals.

In (5),  $\exp(-RB^2/\beta^2)$  is typically used for removing blob-like and systematic random noise signals. However, since the systematic random noises are removed by MDoG and there is no blob-like structure in ocular imaging, we modify (5) as follows:

$$I(\sigma) = \begin{cases} 0, & \lambda_2 > 0 \text{ or } \lambda_3 > 0 \\ \left(1 - \exp\left(-\frac{RA^2}{2\alpha^2}\right)\right) \times \left(1 - \exp\left(-\frac{S^2}{2\gamma^2}\right)\right), & \text{else} \end{cases} \quad (6)$$

where  $\alpha$  is fixed to 0.5 to enable better smoothing effect of the filter, and  $\gamma$  is related to the dynamic range of the grayscale image, which is usually set around  $S/2$ . This simplification of the equation improves the calculation speed of this filter.

The final feature map, i.e., the 3D map of enhanced vascular signals, is obtained by comparing every voxel of all the feature maps calculated with different  $\sigma$ , and choosing the one with the maximum response:

$$I' = \max_{\sigma_{\min} \leq \sigma \leq \sigma_{\max}} |I(\sigma)| \quad (7)$$

where  $\sigma_{\min} = 1$  and  $\sigma_{\max} = 9$  are different kernel sizes chosen in this study, which were determined by the distribution of the vessel diameter.

**2.4.4 Exponential Transformation Function:** To further enhance the microvasculature signals, an exponential transformation function was applied to the feature map  $I'(x, y, z)$  to obtain the vascular enhancement data  $V(x, y, z)$ :

$$V(x, y, z) = I'(x, y, z)^r \quad (8)$$

where  $r$  is an adjustable parameter, which was empirically set between 0.3 and 0.5 to control the threshold range.

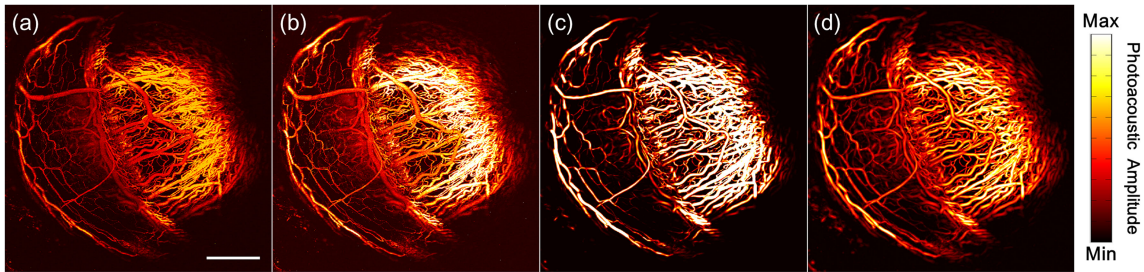


Fig. 4. (a) The original MAP image. (b) The normalized MAP image. (c) The filtered MAP image by the modified Frangi's filter. (d) The filtered MAP image by the exponential transformation function. The color bar indicates the photoacoustic amplitude. Scale bar = 1 mm.

**2.4.5 Oxygen Saturation of Hemoglobin ( $sO_2$ ) Map Calculating:** Based on the optical absorption of oxy-hemoglobin and deoxy-hemoglobin at 532 nm and 560 nm, respectively, the relative concentration,  $sO_2(x, y, z)$ , of each component is derived voxel-by-voxel using:

$$sO_2(x, y, z) = \frac{C_{oxy}(x, y, z)}{C_{oxy}(x, y, z) + C_{deoxy}(x, y, z)} \times 100\% \quad (9)$$

where  $C_{oxy}$  is the concentration of oxy-hemoglobin and  $C_{deoxy}$  is the concentration of deoxy-hemoglobin.

The vascular enhancement data obtained using the PAIVEF are used as the mask to calculate the final  $sO_2$  map:

$$MAPsO_2 = \max(sO_2(x, y, z) \cdot V(x, y, z), [], 3) \quad (10)$$

where  $\max(a(x, y, z), [], 3)$  means calculate the maximum amplitude projection (MAP) image of the 3D volume in the depth ( $z$ ) direction.

### 3. Results and Discussion

The series of enhanced images for each step using our filter is shown in Fig. 4. The original MAP image, the normalized MAP image, the MAP image filtered by the modified Frangi's filter, and the MAP image filtered by the exponential transformation function are shown in Figs. 4(a) through 4(d), respectively. The enhanced vasculature signal obtained using modified Frangi's filter while suppressing the background signal is shown in Fig. 4(c). In Fig. 4(d), further enhancement of weaker vascular signals (such as the microvessels and the blood vessels farther away from the focus area) using the exponential transformation function is shown. The intensity of microvessels is close to that of big vessels after the exponential transformation, which is beneficial to further vasculature extraction. It is worth noting that the visually weaker blood vessels in Fig. 4(a) appear thicker in Fig. 4(d). It is mainly because the weak vascular signals in original data are enhanced and with this enhancement the differences in intensity between the weak vascular signals and the strong vascular signals become small. This process is further explained through Figs. 5(i) and 5(j) in the next paragraph.

Figs. 5(a)–5(e) show original MAP image, MAP images filtered by three previously published algorithms ([33], [34], [40]), and our algorithm, respectively. The enlarged images of three outlined regions in Fig. 5(a) are shown in Figs. 5(f1), 5(g1), and 5(h1). These three regions shift from in-focus to defocus plane in 3D volume, and are outlined using green dashed rectangles in Fig. 5(a) and numbered 1, 2, and 3. Corresponding enlarged images of Figs. 5(b)–5(e), belonging to the same regions as outlined in Fig. 5(a), are shown in 5(f2)–5(f5), 5(g2)–5(g5), and 5(h2)–5(h5). As can be seen from Figs. 5(f1)–5(f5), for the in-focus plane, except the partial microvascular signal missing in Fig. 5(f4) (shown by the blue arrow), both the other two previous methods and our method have a good effect on the blood vessel enhancement. However, for the defocus plane,



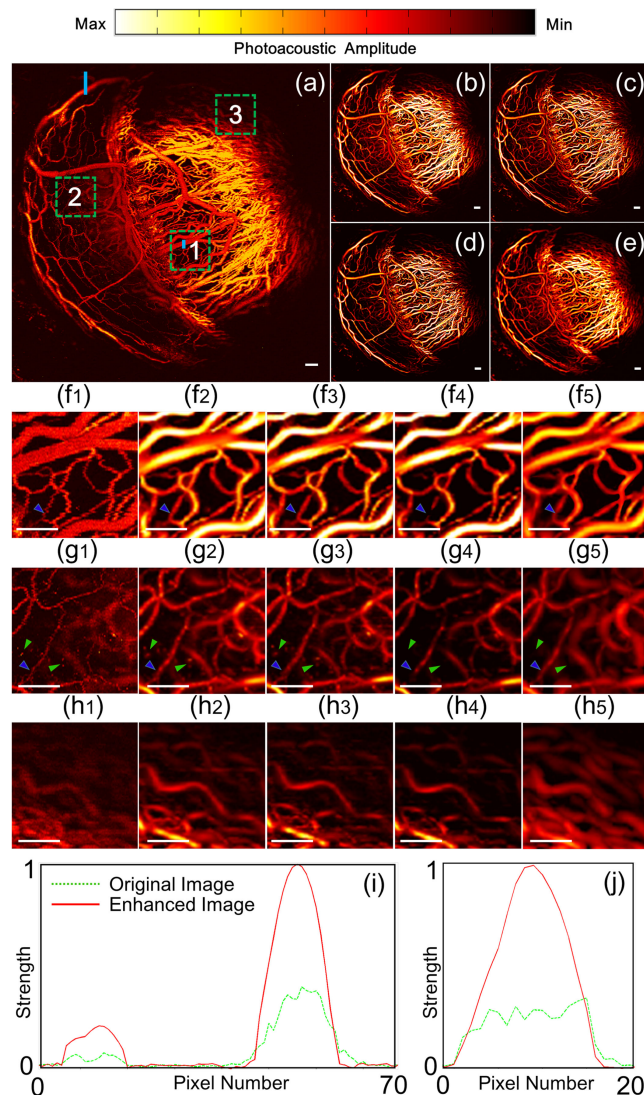


Fig. 5. (a) The original MAP image. (b)–(e) The filtered MAP image by [33], [34], [40], and our algorithm, respectively. (f1)–(f5) The same enlarged area in (a)–(e), this area is pointed out by green dotted frame 1. (g1)–(g5) The same enlarged area in (a)–(e), this area is pointed out by green dotted frame 2. (h1)–(h5) The same enlarged area in (a)–(e), this area is pointed out by green dotted frame 3. (i) The strength values of the same part in (a) and (e), this part is plotted by the longer blue solid line in (a), the green dashed line and the red solid line represent the strength values of (a) and (e) in this part, respectively. (j) The strength values of the same part in (a) and (e), this part is plotted by the shorter blue solid line in (a), the green dashed line and the red solid line represent the strength values of (a) and (e) in this part, respectively. The color bar indicates the photoacoustic amplitude of (a)–(h). Scale bar = 200  $\mu\text{m}$ .

as shown in Figs. 5(g2) and 5(g3), the speckled noise signals (some of them are indicated by the green arrows) are also enhanced in addition to the enhancement of the vascular signal. In Fig. 5(g4), some microvascular signals (shown by the blue arrow) are not enhanced. Our method as shown in Fig. 5(g5) shows the best images, wherein the enhancement of the vascular signals takes place while suppressing the noise signals. Figs. 5(h1)–5(h5) shows the results for the farther defocused plane. As shown in Figs. 5(h2)–5(h4) for the three previous methods, the vascular signals are enhanced unevenly for different regions in the image, and the diameter of partial vessels are reduced compared to the raw image in Fig. 5(h1). While with our method, as shown in Fig. 5(h5),

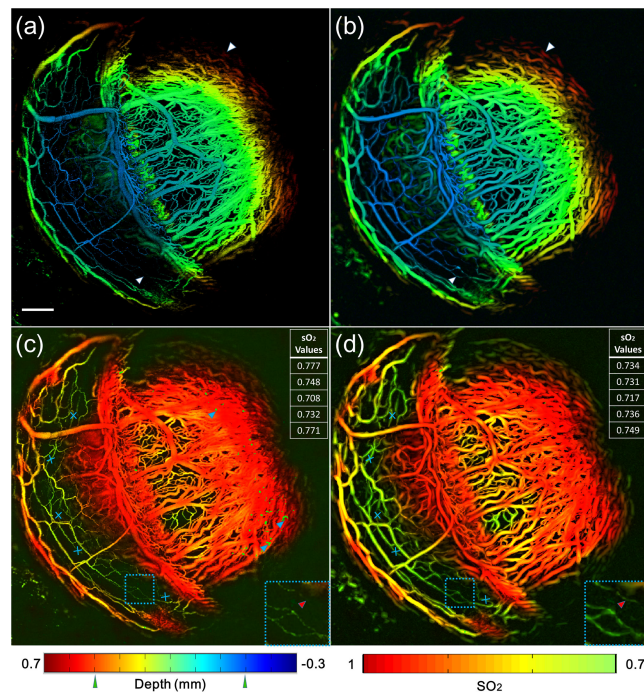


Fig. 6. (a) Depth encoded MAP image of the original data. (b) Depth encoded MAP image of the data enhanced by our filter. (c) The sO<sub>2</sub> MAP image of the rat ocular anterior segment using the original data as mask. (d) The sO<sub>2</sub> MAP image of the rat ocular anterior segment using the enhanced data as mask. The values in (c) and (d) are the sO<sub>2</sub> values at the five blue crossings in each figure. The color bar on the left indicates depth information of (a) and (b). The color bar on the right indicates sO<sub>2</sub> values of (c) and (d). Scale bar = 500  $\mu$ m.

the vascular signals are enhanced evenly throughout the image and the vascular diameters are recovered accurately. Even when the intensities of vascular signals are weak in the defocus area, our algorithm can still enhance the large vessels with low SNR. To further verify the accuracy of the enhanced vascular signals by our filter from the in-focus to defocus plane, the signal strength along the two blue solid lines indicated in Fig. 5(a) (each representing in-focus and defocus plane) are plotted and shown in Figs. 5(i) and 5(j) as green dotted lines. The corresponding same plots for the vascular enhanced image using our method (i.e., Fig. 5(e)) are shown in Figs. 5(i) and 5(j) as red solid lines. It is worth noting that accurate enhancement of defocus vasculature has always been a challenge. In order to verify that our algorithm can accurately enhance the blood vessels in the defocus plane, two blood vessels with different diameters and signal strengths in the defocus region are covered by the relatively longer blue line shown in Fig. 5(a) and their intensity profiles are plotted. As can be seen in Figs. 5(i) and 5(j), accurate vascular signal enhancement in 5(e) takes place in both in-focus and defocus areas. This confirms the ability of our algorithm to suppress the noise signals while accurately extracting blood vessels from in-focus to defocus planes in OR-PAM images and have better performance than other filters in the literature.

The improved enhancement of the vascular signals by our algorithm is attributed to the following points: 1. The MDoG function combined with the modified Frangi's filter not only smooths the blood vessel signals of different diameters at multiple scales but also removes the high-frequency noise signals while enhancing the microvascular signals. 2. An exponential transformation function built into the algorithm further increases the microvascular signals, minimizing the intensity differences between the microvascular and other vascular signals.

Figs. 6(a) and 6(b) show the depth encoded MAP images of the original data and the vascular enhancement data, respectively. It can be seen in Fig. 6(a), the weak signals, marked by white

arrows, far away from the focal plane (i.e., red and blue colors) are obscured by the background and are difficult to identify. However, in Fig. 6(b), these signals can be clearly identified due to the enhancement of the vasculature by our algorithm. Combining our vascular enhancement algorithm with the custom-built OR-PAM, we could achieve highly sensitive and accurate anterior segment photoacoustic imaging of the vasculature at a large depth range ( $\sim 0.6$  mm, which was  $\sim 7$  times of the systems DOF). The depth range in Figs. 6(a) is indicated by two green triangular arrows beneath the scale bar. With our technique, the anterior segment of the eye and other arc-shaped vasculature can be scanned while providing accurate 3D positioning of local blood vessels to facilitate monitoring of the lesion area. Figs. 6(c) and 6(d) show the sO<sub>2</sub> results of anterior segment using original and enhanced data as mask. The calculated sO<sub>2</sub> values agree well with the previously reported studies [22], [44], [45]. Compared to Fig. 6(c), the result in Fig. 6(d) using vascular-enhanced MAP as mask has the following advantages: (1) The SNR in Fig. 6(d) is higher than that in Fig. 6(c). As can be seen from the enlarged blue dotted box, the blood vessel indicated by the red arrow is obscured by the background in Fig. 6(c) but can be clearly seen in Fig. 6(d). Meanwhile the vessels in the blue dotted box are more continuous in Fig. 6(d) compared to Fig. 6(c). (2) Random speckles indicated by the blue arrows only exist in Fig. 6(c) but not in Fig. 6(d). (3) The gradual decrease of sO<sub>2</sub> values in Fig. 6(d) is smoother than that in Fig. 6(c), which agrees with the true physiological status. To quantitatively validate the accuracy of our method, five capillaries with sO<sub>2</sub> values on the same level but at different depths (indicated by five blue crossings in Fig. 6(c) and (d) in the revised manuscript) are selected for sO<sub>2</sub> value calculation. The corresponding values are showed in the upper right corner of Fig. 6(c) and (d), respectively. It can be seen that the values are more close to each other in Fig. 6(d) (0.717–0.749) compared to Fig. 6(c) (0.708–0.777) due to the enhancement of the photoacoustic images, which indicates the accuracy of our algorithm.

#### 4. Conclusions

In this study, we used a custom-built OR-PAM to obtain the raw data of the rat anterior segment vasculature and newly developed PAIVEF algorithm to enhance vascular signals of various diameters including microvessels while suppressing high-frequency noise signals within a large depth range in and out of the system's DOF. We successfully demonstrated the utility of the system and algorithm by *in vivo* photoacoustic imaging of the anterior segment vasculature of the rat eyeball. Since the quantitative and functional imaging of blood vessels is the basis for ensuring the accurate diagnosis of ophthalmic vascular disease, our novel vascular enhancement algorithm applied to large depth-range OR-PAM will fill the need of such a clinical system. In the near future, we plan to apply technology developed in this paper to a variety of animal ophthalmic disease models to establish a relationship between vascular morphology and functional changes with the disease courses, providing an efficient and convenient means for disease diagnosis and assessment.

The vascular enhancement algorithm developed in this paper can also be extended to many other applications of photoacoustic imaging where angiography is important, such as brain and back imaging, tumor vasculature imaging. In addition, we believe our algorithm could potentially be extended to other high-resolution imaging modalities such as OCTA, where the need exists to suppress high-frequency noise signals while accurately extracting vasculature signals of different diameters and signal intensities. Thus, our contribution in this paper, would not only enhance PA imaging, but it could also benefit other clinical modality as well.

---

#### References

- [1] T. Vos *et al.*, "Global, regional, and national incidence, prevalence, and years lived with disability for 310 diseases and injuries, 1990-2015: A systematic analysis for the global burden of disease study 2015," *Lancet*, vol. 388, p. 1545, 2016.
- [2] Y.-C. Tham, X. Li, T. Y. Wong, H. A. Quigley, T. Aung, and C.-Y. Cheng, "Global prevalence of glaucoma and projections of glaucoma burden through 2040: A systematic review and meta-analysis," *Ophthalmology*, vol. 121, pp. 2081–2090, 2014.

- [3] Y. Zhang, S. Z. Li, L. Li, M. G. He, R. Thomas, and N. L. Wang, "Dynamic iris changes as a risk factor in primary angle closure disease," *Invest Ophthalmol Vis Sci.*, vol. 57, pp. 218–26, Jan. 01, 2016.
- [4] C. S. Tan *et al.*, "Optical coherence tomography angiography evaluation of the parafoveal vasculature and its relationship with ocular factors," *Invest Ophthalmol Vis Sci.*, vol. 57, pp. OCT224–OCT234, 2016.
- [5] J. G. Ghosh *et al.*, "Long-acting protein drugs for the treatment of ocular diseases," *Nature Commun.*, vol. 8, p. 14837, 2017.
- [6] S. Dithmar and F. G. Holz, *Fluorescence Angiography in Ophthalmology*, Springer Science & Business Media, 2008.
- [7] A. H. Skalet *et al.*, "Optical coherence tomography angiography characteristics of iris melanocytic tumors," *Ophthalmology*, vol. 124, pp. 197–204, 2017.
- [8] M. C. Savastano, B. Lumbroso, and M. Rispoli, "In vivo characterization of retinal vascularization morphology using optical coherence tomography angiography," *Retina*, vol. 35, pp. 2196–2203, 2015.
- [9] F. Ströhl and C. F. Kaminski, "A joint Richardson—Lucy deconvolution algorithm for the reconstruction of multifocal structured illumination microscopy data," *Methods Appl. Fluorescence*, vol. 3, p. 014002, 2015.
- [10] T. E. De Carlo, A. Romano, N. K. Waheed, and J. S. Duker, "A review of optical coherence tomography angiography (OCTA)," *Int. J. Retina Vitreous*, vol. 1, p. 5, 2015.
- [11] P. K. Roberts, D. A. Goldstein, and A. A. Fawzi, "Anterior segment optical coherence tomography angiography for identification of iris vasculature and staging of iris neovascularization: A pilot study," *Current Eye Res.*, pp. 1–7, 2017.
- [12] W. J. Choi, Z. Zhi, and R. K. Wang, "In vivo OCT microangiography of rodent iris," *Opt. Lett.*, vol. 39, pp. 2455–2458, 2014.
- [13] C. Tian, W. Zhang, A. Mordovanakis, X. Wang, and Y. M. Paulus, "Noninvasive chorioretinal imaging in living rabbits using integrated photoacoustic microscopy and optical coherence tomography," *Opt. Exp.*, vol. 25, pp. 15947–15955, 2017.
- [14] J. G. Laufer *et al.*, "In vivo preclinical photoacoustic imaging of tumor vasculature development and therapy," *J. Biomed. Opt.*, vol. 17, p. 056016, 2012.
- [15] J. Yao *et al.*, "High-speed label-free functional photoacoustic microscopy of mouse brain in action," *Nature Methods*, vol. 12, p. 407, 2015.
- [16] R. Cao *et al.*, "Functional and oxygen-metabolic photoacoustic microscopy of the awake mouse brain," *Neuroimage*, vol. 150, pp. 77–87, 2017.
- [17] H. Zhao *et al.*, "Motion correction in optical resolution photoacoustic microscopy," *IEEE Trans. Med. Imag.*, vol. 38, no. 9, pp. 2139–2150, Sep. 2019.
- [18] A. Krumholz, L. Wang, J. Yao, and L. V. Wang, "Functional photoacoustic microscopy of diabetic vasculature," *J. Biomed. Opt.*, vol. 17, p. 060502, 2012.
- [19] L. V. Wang and S. Hu, "Photoacoustic tomography: In Vivo imaging from organelles to organs," *Sci. (New York, Ny)*, vol. 335, p. 1458, 2012.
- [20] A. Taruttis and V. Ntziachristos, "Advances in real-time multispectral optoacoustic imaging and its applications," *Nature Photon.*, vol. 9, p. 219, 2015.
- [21] W. Liu and H. F. Zhang, "Photoacoustic imaging of the eye: A mini review," *Photoacoustics*, vol. 4, pp. 112–123, 2016.
- [22] S. Hu, B. Rao, K. Maslov, and L. V. Wang, "Label-free photoacoustic ophthalmic angiography," *Opt. Lett.*, vol. 35, pp. 1–3, 2010.
- [23] W. Zhang *et al.*, "High-resolution, in vivo multimodal photoacoustic microscopy, optical coherence tomography, and fluorescence microscopy imaging of rabbit retinal neovascularization," *Light: Sci. Appl.*, vol. 7, p. 103, 2018.
- [24] N. Wu, S. Ye, Q. Ren, and C. Li, "High-resolution dual-modality photoacoustic ocular imaging," *Opt. Lett.*, vol. 39, pp. 2451–4, Apr. 15, 2014.
- [25] W. Liu *et al.*, "In vivo corneal neovascularization imaging by optical-resolution photoacoustic microscopy," *Photoacoustics*, vol. 2, pp. 81–86, 2014.
- [26] A. de La Zerda *et al.*, "Photoacoustic ocular imaging," *Opt. Lett.*, vol. 35, pp. 270–272, 2010.
- [27] B. Rao, L. Li, K. Maslov, and L. Wang, "Hybrid-scanning optical-resolution photoacoustic microscopy for in vivo vasculature imaging," *Opt. Lett.*, vol. 35, pp. 1521–1523, 2010.
- [28] S. Jeon *et al.*, "In vivo photoacoustic imaging of anterior ocular vasculature: A random sample consensus approach," *Scientific Reports*, vol. 7, p. 4318, 2017.
- [29] S. Avtzi, G. J. Tservelakis, M. K. Tsilimbaris, and G. Zacharakis, "Delineating the anatomy of the ciliary body using hybrid optical and photoacoustic imaging," *J. Biomed. Opt.*, vol. 22, p. 060501, 2017.
- [30] H. Duadi, D. Fixler, and R. Popovtzer, "Dependence of light scattering profile in tissue on blood vessel diameter and distribution: A computer simulation study," *J. Biomed. Opt.*, vol. 18, p. 111408, 2013.
- [31] H. Duadi, M. Nitzan, and D. Fixler, "Simulation of oxygen saturation measurement in a single blood vein," *Opt. Lett.*, vol. 41, pp. 4312–4315, 2016.
- [32] T. Jerman, F. Pernuš, B. Likar, and Ž. Špiclin, "Beyond Frangi: An improved multiscale vesselness filter," in *Med. Image 2015: Image Process.*, 2015, p. 94132A.
- [33] Y. Sato *et al.*, "Tissue classification based on 3D local intensity structures for volume rendering," *IEEE Trans. Visualization Comput. Graph.*, vol. 6, pp. 160–180, Apr.-Jun. 2000.
- [34] Q. Li, S. Sone, and K. Doi, "Selective enhancement filters for nodules, vessels, and airway walls in two-and three-dimensional CT scans," *Med. Phys.*, vol. 30, pp. 2040–2051, 2003.
- [35] A. F. Frangi, W. J. Niessen, K. L. Vincken, and M. A. Viergever, "Multiscale vessel enhancement filtering," in *Proc. Int. Conf. Med. Image Comput. Comput.-Assisted Intervention*, 1998, pp. 130–137.
- [36] A. Camino *et al.*, "Automated registration and enhanced processing of clinical optical coherence tomography angiography," *Quantitative Imag. Medicine Surgery*, vol. 6, p. 391, 2016.
- [37] J. de Moura, J. Novo, P. Charlón, N. Barreira, and M. Ortega, "Enhanced visualization of the retinal vasculature using depth information in OCT," *Med. Biol. Eng. Comput.*, vol. 55, pp. 2209–2225, 2017.

- [38] P. Li, Z. Huang, S. Yang, X. Liu, Q. Ren, and P. Li, "Adaptive classifier allows enhanced flow contrast in OCT angiography using a histogram-based motion threshold and 3D Hessian analysis-based shape filtering," *Opt. Lett.*, vol. 42, pp. 4816–4819, 2017.
- [39] H. F. Zhang, K. Maslov, M.-L. Li, G. Stoica, and L. V. Wang, "In vivo volumetric imaging of subcutaneous microvasculature by photoacoustic microscopy," *Opt. Exp.*, vol. 14, pp. 9317–9323, 2006.
- [40] H. Zhao *et al.*, "Three-dimensional Hessian matrix-based quantitative vascular imaging of rat iris with optical-resolution photoacoustic microscopy in vivo," *J. Biomed. Opt.*, vol. 23, p. 046006, 2018.
- [41] C. Yeh, B. Soetikno, S. Hu, K. I. Maslov, and L. V. Wang, "Three-dimensional arbitrary trajectory scanning photoacoustic microscopy," *J. Biophotonics*, vol. 8, pp. 303–308, 2015.
- [42] C. Yeh, B. T. Soetikno, S. Hu, K. I. Maslov, and L. V. Wang, "Microvascular quantification based on contour-scanning photoacoustic microscopy," *J. Biomed. Opt.*, vol. 19, p. 096011, 2014.
- [43] J. Chen, R. Lin, H. Wang, J. Meng, H. Zheng, and L. Song, "Blind-deconvolution optical-resolution photoacoustic microscopy in vivo," *Opt. Exp.*, vol. 21, pp. 7316–7327, 2013.
- [44] A. Geirsdottir, O. Palsson, S. H. Hardarson, O. B. Olafsdottir, J. V. Kristjansdottir, and E. Stefánsson, "Retinal vessel oxygen saturation in healthy individuals," *Investigative Ophthalmology Visual Sci.*, vol. 53, pp. 5433–5442, 2012.
- [45] S. N. Hennen *et al.*, "Photoacoustic tomography imaging and estimation of oxygen saturation of hemoglobin in ocular tissue of rabbits," *Exp. Eye Res.*, vol. 138, pp. 153–158, 2015.